ACSNANO

www.acsnano.org

ARTICLE

Fate of Antibody-Targeted Ultrasmall Gold Nanoparticles in Cancer Cells after Receptor-Mediated Uptake

Sangheon Han, Tomasz Zal,* and Konstantin V. Sokolov*

Cite This: *ACS Nano* 2021, 15, 9495–9508

Read Online

ACCESS | Metrics & More | Article Recommendations | Supporting Information

ABSTRACT: **Nanoparticles with ultrasmall sizes (less than 10 nm) offer many advantages in biomedical applications compared to their bigger counterparts, including better intratumoral distribution, improved pharmacokinetics (PK), and efficient body clearance. When functionalized with a biocompatible coating and a target-specific antibody, ultrasmall nanoparticles represent an attractive clinical translation platform. Although there is a tremendous body of work dedicated to PK and the biological effects of various nanoparticles, little is known about the fate of different components of functionalized nanoparticles in a biological environment such as in live cells. Here, we used luminescence properties of 5 nm gold nanoparticles (AuNPs) to study the intracellular trafficking and fate of the AuNPs functionalized with an organic layer consisting of a polyethylene glycol (PEG) coating and epidermal growth factor receptor (EGFR)-targeting antibody. We showed that intracellular uptake of the targeted 5 nm AuNPs results in a strong two-photon luminescence (TPL) that is characterized by broad emission and very short lifetimes compared to the fluorescence of the nanoparticle-conjugated fluorophore-tagged antibody, thereby allowing selective imaging of these components using TPL and two-photon excited fluorescence lifetime microscopy (2P-FLIM). Our results indicate that the nanoparticle's coating is detached from the particle's surface inside cells, leading to formation of nanoparticle clusters with a strong TPL. Furthermore, we observed an optically resolved spatial separation of the gold core and the antibody coating of the particles inside cells. We used data from two-photon microscopy, 2P-FLIM, electron microscopy, and *in vitro* assays to propose a model of interactions of functionalized 5 nm AuNPs with live cells.**

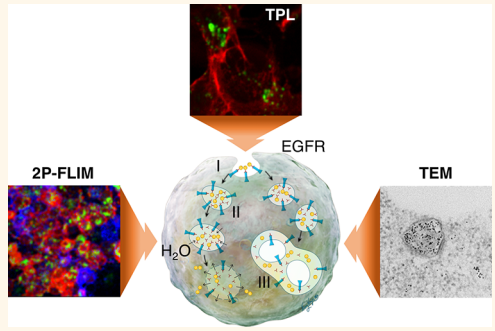

KEYWORDS: *hybrid nanoparticles, two-photon microscopy, fluorescence lifetime imaging, colocalization, ultrasmall nanoparticles, molecular imaging*

Development of nanoparticles for biomedical applications commonly requires designing multicomponent hybrid structures to achieve a desired function in a complex biological environment. Nanoparticle cores commonly consist of either organic materials such as polymers[1−3] and lipids[4−8] or inorganic elements including gold, silver, semiconductor, and iron oxide.[9−16] Further, the cores can include a mixture of various organic and inorganic materials with imaging and therapeutic functionalities.[17−22] Nanoparticle surface coatings are aimed at providing stability, including protection from opsonization and biofouling, and often include moieties such as peptides or antibodies to enable specific binding to biological targets such as cancer cells.[23−26]

A tremendous amount of research has been aimed at understanding and manipulating nanoparticle toxicity, targeting, biodistribution, and excretion in various biomedical applications.[27−31] Of particular interest is the intracellular fate of nanoparticles targeted through specific cell surface binding to accumulate in the cell's interior. Many studies had focused on the fate of a single component of hybrid nanoparticles (e.g., an inorganic core).[32−34] However, it has been well-established that hybrid nanoparticles, which are stable in solution or even serum, can lose their integrity in complex biological environments, particularly after cellular uptake. Once internalized, nanoparticles are subjected to intracellular trafficking, accompanied by significant changes in the local chemical environment.[35] A gradual decrease in pH values in endosomal pathways and the presence of proteolytic

Received: September 26, 2020
Accepted: May 12, 2021
Published: May 20, 2021

https://doi.org/10.1021/acsnano.0c08128
ACS Nano 2021, 15, 9495−9508

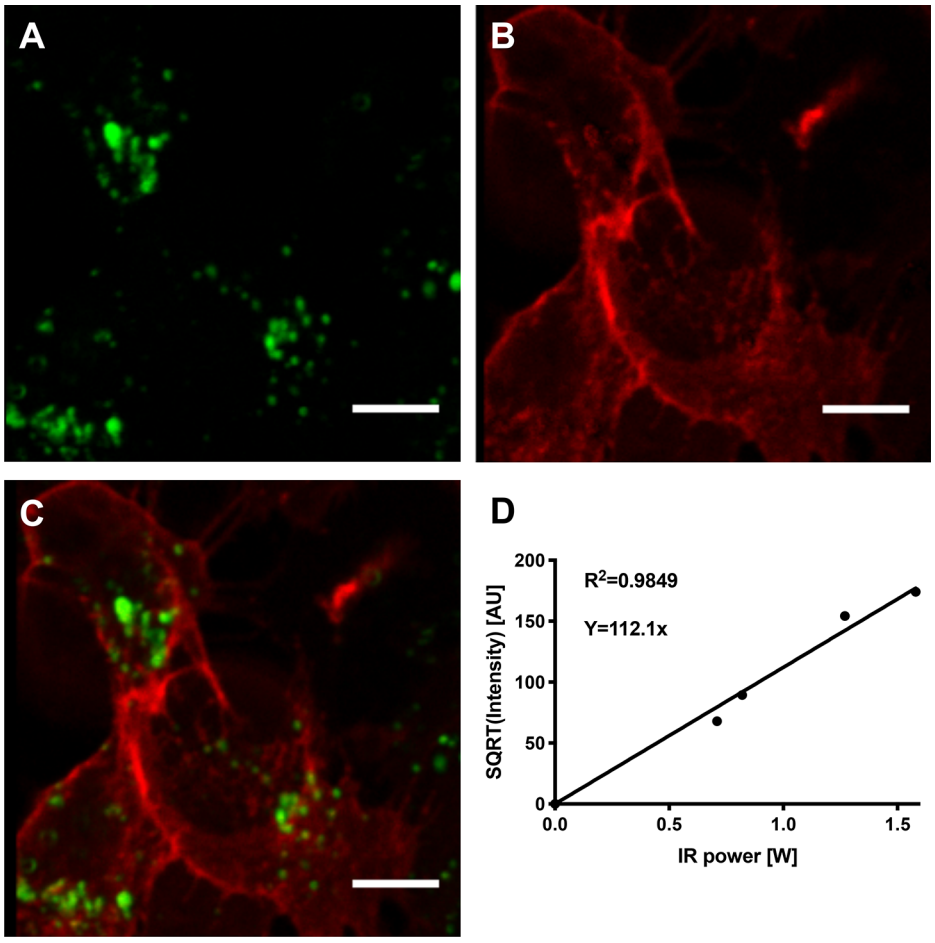

Figure 1. Two-photon fluorescence images of A431 cells after incubation with 5 nm aEGFR-AuNPs for 24 h showing (A) luminescence from 5 nm aEGFR-AuNPs, (B) fluorescence from CellLight Plasma Membrane-CFP BacMam 2.0, and (C) overlay of the two signals. Green color indicates 5 nm AuNP luminescence, and red corresponds to the CFP fluorescence. (D) Quadratic dependence of the luminescence signal from AuNPs on the incident femtosecond-pulsed laser average power at 880 nm wavelength. Scale bars are 15 μm.

enzymes and reactive oxygen species can adversely (or usefully) affect the integrity of organic components, resulting in a slow decomposition of some inorganic materials (*e.g.*, iron oxide).[36,37] Further, elevated concentration of some biomolecules inside cells, such as glutathione (GSH), may lead to disruption of chemical bonds, including thiol binding to the gold surface or disulfides.[38] Little is known about the relative fates of the nanoparticle core *versus* the organic components of hybrid nanoparticles after their cellular uptake or *in vivo* administration. This knowledge is critical in further developing multicomponent nanoparticles for biomedical applications, as it could provide innovative design ideas, such as improving therapeutic efficacy, imaging contrast, and nanoparticle clearance and limiting off-target toxicity *in vivo*.

Comprehensive studies focused on examination of the fate of different components of functionalized nanoparticles include a dual-labeling technique that was recently implemented to independently monitor the biodistribution of a core and a shell of polymer-coated gold nanoparticles (AuNPs) where the gold core contained ^{198}Au radioactive isotope and the polymer shell was labeled with ^{111}In.[39] Levels of radioactivity were measured from excised organs, blood, urine, and feces collected at different time points postinjection into normal rats using γ-spectrometry. It was shown that the hybrid gold nanoparticles were partially degraded *in vivo* with cores and shells having different biodistribution patterns. In a follow-up study, polymer coating of quantum dots (Qdots) and physisorbed human serum albumins (HSA) were labeled using two dyes with distinct fluorescence maxima to observe intracellular fate and exocytosis of these tricomponent particles (polymer, Qdots, HSA) over 72 h.[40] Using flow cytometry and confocal microscopy, this study indicated that HSA was desorbed from the surface of Qdots faster than the polymer coating degradation inside HeLa cells. Further, each component was exocytosed by the cells at a different rate. Such quantitative experiments are the first step in understanding how complex hybrid nanostructures are processed by cells that provide a foundation for evaluating *in vivo* scenarios.

Here, we used two-photon luminescence (TPL) to investigate the fate of antibody-conjugated spherical AuNPs with ultrasmall 5 nm gold cores targeted to epidermal growth factor receptor (EGFR) (5 nm aEGFR-AuNPs) after receptor-mediated uptake by cancer cells. This study was motivated by our and others' interest in developing inorganic nanoparticles with core dimensions less than 10 nm for potential clinical applications.[41−43] Nanoparticles in this size range have several significant advantages over their bigger counterparts, including longer circulation time, improved biodistribution, and better tissue penetration.[44] Furthermore, the ultrasmall particles can be efficiently excreted *via* renal and bile clearance pathways that can significantly reduce the toxicity associated with

https://doi.org/10.1021/acsnano.0c08128
ACS Nano 2021, 15, 9495−9508

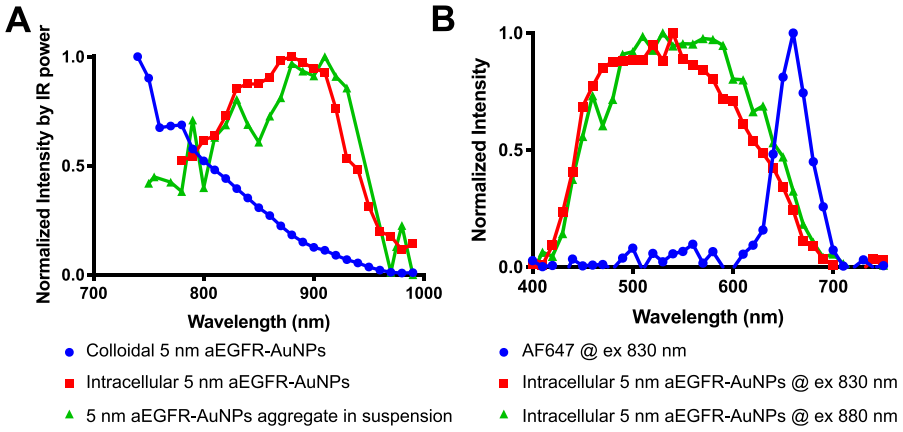

Figure 2. Excitation and emission spectra of 5 nm AuNPs in labeled cancer cells and in suspension. (A) Two-photon luminescence excitation spectra of colloidal 5 nm aEGFR-AuNPs (blue); intracellular 5 nm aEGFR-AuNPs (red); and 5 nm aEGFR-AuNP aggregates in suspension (green); all spectra are normalized to one at their corresponding maxima. The emission was measured using a 560−680 nm filter. (B) Two-photon emission spectra of intracellular 5 nm aEGFR-AuNPs and AF647-labeled antibodies. Excitation wavelengths: 830 (red) and 880 (green) nm for 5 nm aEGFR-AuNPs and 830 nm for AF647 (blue).

prolonged body accumulation[45] and, thereby, can improve clinical translation potential.

RESULTS AND DISCUSSION

Two-Photon Luminescence of Antibody-Targeted Gold Nanoparticles. We previously described the 5 nm aEGFR-AuNPs used in this study.[41] Briefly, anti-EGFR antibodies were conjugated to 5 nm AuNPs using directional conjugation chemistry through a periodate-oxidated carbohydrate antibody moiety and a bifunctional linker with a dithiol group for a stronger attachment to the gold surface.[41,46] The particles had the optical absorbance maximum at ∼516 nm that was shifted to ∼524 nm after conjugation of anti-EGFR monoclonal antibodies labeled with AF647 fluorescent dye. The number of antibodies per gold core was 2.7 on average, estimated based on the AF647 absorption peak at 650 nm, the AuNP absorption at 524 nm, and known extinction coefficients of the fluorescently labeled antibodies and the nanoparticles. The hydrodynamic diameter of the spherical AuNPs changed from 7 ± 2 nm to 22 ± 6 nm after antibody conjugation. TEM images of aEGFR-AuNPs showed core sizes with a ∼5 nm diameter (Supplementary Figure 1). Size-exclusion chromatography confirmed complete removal of free antibodies after washing of the conjugates by ultracentrifugation.[41]

Our first goal was to image the AuNP cores with a high degree of signal specificity and sensitivity inside living cells. Initially, we attempted this using confocal reflectance microscopy, relying on the phenomenon of light scattering by AuNP cores. However, we found that this approach provided only low image contrast due to a relatively strong background scattering from cellular organelles (data not shown). Previously, it was shown that gold nanoparticles exhibit a strong, shape-dependent TPL[47−50] that can be used for high-contrast imaging of AuNPs in cells.[51] Therefore, we explored the technique of TPL in which AuNPs are induced to emit light upon two-photon absorption of light from a femtosecond-pulsed laser. In this regime, cellular background signals are small, and fluorescence is selectively detected at specific wavelengths of endogenous chromophores. Cancer cells were transfected to express a cyan fluorescent protein (CFP) on their membranes and were incubated with 5 nm aEGFR-AuNPs at a 2.36 μg/mL concentration for 24 h. No cellular cytotoxicity was observed for 5 nm aEGFR-AuNPs up to 75 μg/mL (Supplementary Figure 2). Cellular uptake of 5 nm aEGFR-AuNPs was associated with strong TPL (Figure 1A−C). The intensity of luminescence had a quadratic dependence on the excitation power (Figure 1D), confirming a nonlinear, two-photon process. Considering prior work showing that spherical AuNPs have a relatively low two-photon cross-section compared to nonspherical shapes,[52] we wanted to determine whether TPL from our 5 nm aEGFR-AuNPs was coming from individual particles or their clusters. For this purpose, we compared the TP excitation spectra of intracellular 5 nm aEGFR-AuNPs with the TP spectra of colloidal (unaggregated) 5 nm aEGFR-AuNPs and the TP spectra of a suspension of uncoated 5 nm AuNP core aggregates (Figure 2A). In addition, we compared the TP excitation spectra of intracellular 5 nm aEGFR-AuNPs with that of the targeted particles that were cross-linked *in vitro* using the NHS-PEG-NHS molecules. We found that the clustering of 5 nm aEGFR-AuNPs led to an increase in their red-NIR absorbance comparable to the absorbance of aggregates of 5 nm AuNP cores (Supplementary Figure 3). The TP excitation spectra of the colloidal unaggregated *versus* the intracellular 5 nm aEGFR-AuNPs were strikingly different (Figure 2A). However, both the cross-linked 5 nm aEGFR-AuNPs and aggregated 5 nm AuNP cores in suspension exhibited practically identical TP excitation spectra to the signals from intracellular 5 nm aEGFR-AuNPs (Figure 2A). These data indicated that the TP signals from 5 nm aEGFR-AuNPs in cancer cells came from AuNP aggregates or clusters of AuNPs inside endosomes rather than individual particles. While colloidal 5 nm aEGFR-AuNPs showed TP excitation spectra (Figure 2A) that resembled the profile of their absorbance spectra (Supplementary Figure 3), the intracellular 5 nm aEGFR-AuNPs exhibited an increased excitation efficiency between 830 and 920 nm with a peak at ∼880 nm (Figure 2A). Moreover, intracellular 5 nm aEGFR-AuNPs had a ∼46-fold brighter TPL signal than individual colloidal particles at 880 nm excitation. Also, emission spectra of the intracellular 5 nm aEGFR-AuNPs showed broad luminescence emission in the 400 to 700 nm region when excited at 830 and 880 nm (Figure 2B). Interestingly, this broad emission spectrum was similar to the TP emission of NIR-absorbing AuNPs such as gold

https://doi.org/10.1021/acsnano.0c08128
ACS Nano 2021, 15, 9495−9508

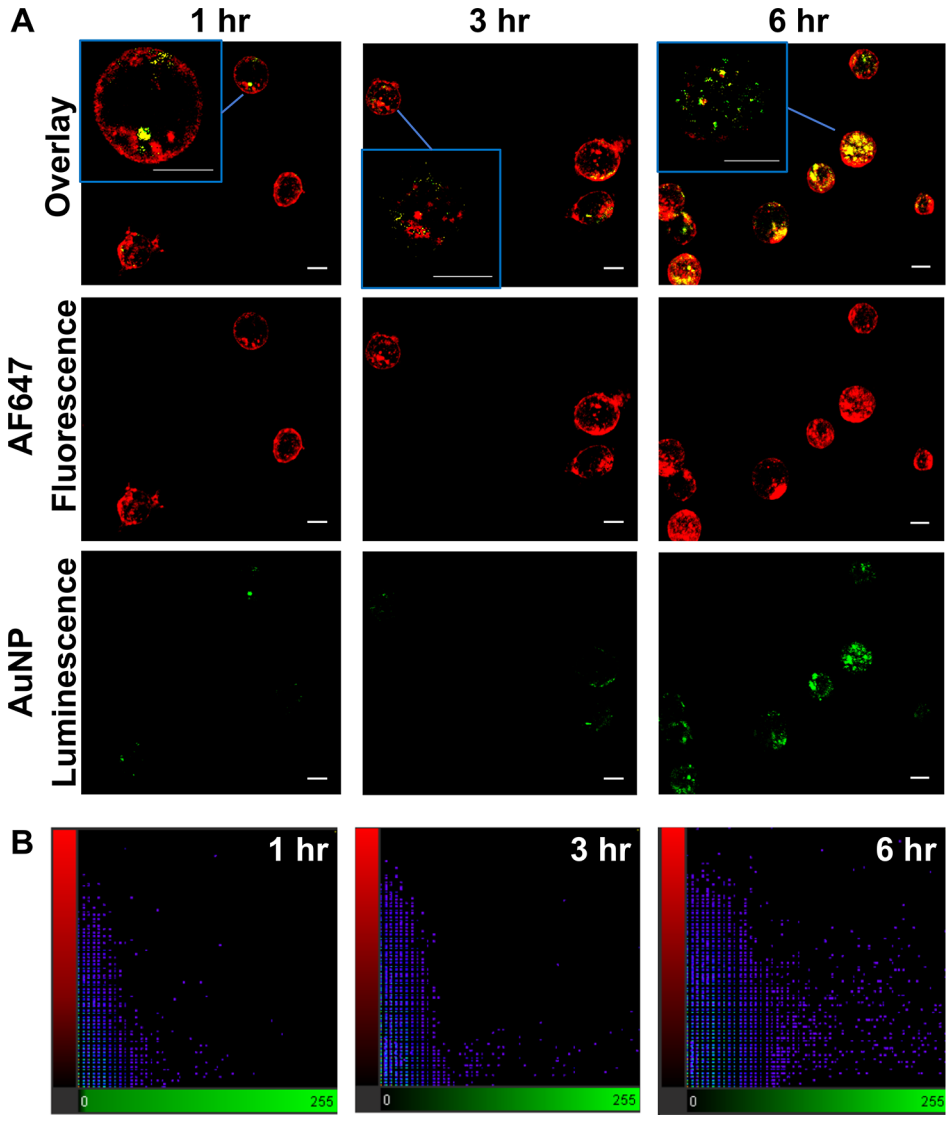

Figure 3. Two-photon microscopy imaging of 5 nm aEGFR-AuNPs in A431 cells. (A) Time-course maximum projection images at 1, 3, and 6 h after addition of 5 nm aEGFR-AuNPs to cells; the nanoparticles were conjugated with AF647-labeled anti-EGFR antibodies. The magnified cross-sectional images (insets) in the top row show colocalization between AuNP (green) and antibodies (red); the yellow color indicates colocalized voxels with AuNPs and antibodies. Scale bars are 20 μm. (B) Corresponding intensity scatterplots for 5 nm AuNP luminescence (green, *x*-axis) and the fluorescence from AF647 (red, *y*-axis) from TPL images.

nanocages[53] and gold nanorods.[50] Note that there was no detectable signal from unlabeled cells under the same imaging conditions that were used to image intracellular antibody-conjugated nanoparticles.

As mentioned above, spherical AuNPs were shown to have the lowest TPL cross-section compared to other shape types such as gold nanocages, nanorods, and nanostars.[52] It is also known that the efficiency of TPL of spherical AuNPs is greatly increased in assemblies of spherical AuNPs due to the plasmon resonance coupling effect.[47,54] This assembly-mediated enhancement of TPL is strongly dependent on the interparticle distance with an enhancement factor of ~115-fold reported for 21 nm diameter spherical AuNPs separated by 2.0 nm edge-to-edge. The enhancement factor decreased to ~4.0 at the 12.2 nm separation.[54] Together with these previous reports, our above-mentioned data provide strong support to the conclusion that the TPL from intracellular 5 nm aEGFR-AuNPs was due to the local formation of closely spaced gold nanoparticle clusters.

Emission spectra of AF647 at 830 nm TP excitation had a minimum overlap with the emission from intracellular 5 nm aEGFR-AuNPs (Figure 2B). Therefore, we selected AF647 to label the AuNP-conjugated antibodies and to independently monitor the fate of antibodies and 5 nm AuNP cores following cellular uptake of 5 nm aEGFR-AuNPs.

Tracking 5 nm aEGFR-AuNPs in Live Cells Using Two-Photon Microscopy. Three-dimensional TPL images were acquired from cancer cells labeled with 5 nm aEGFR-AuNPs for 1, 3, and 6 h to explore the fate of AuNP conjugates during the early stages of interactions with cells (Figure 3A). Qualitatively, the fluorescence signal from cells had a predominantly circular/spheroidal distribution after 1 h incubation that gradually changed to a more uniform spread inside cells at 3 and 6 h. These changes are likely associated with a progressive trafficking of nanoparticles from the cellular cytoplasmic membrane toward the perinuclear space previously reported for AuNP antibody conjugates.[55] Two-photon microscopy (TPM) images were analyzed using scatterplots

https://doi.org/10.1021/acsnano.0c08128
ACS Nano 2021, 15, 9495−9508

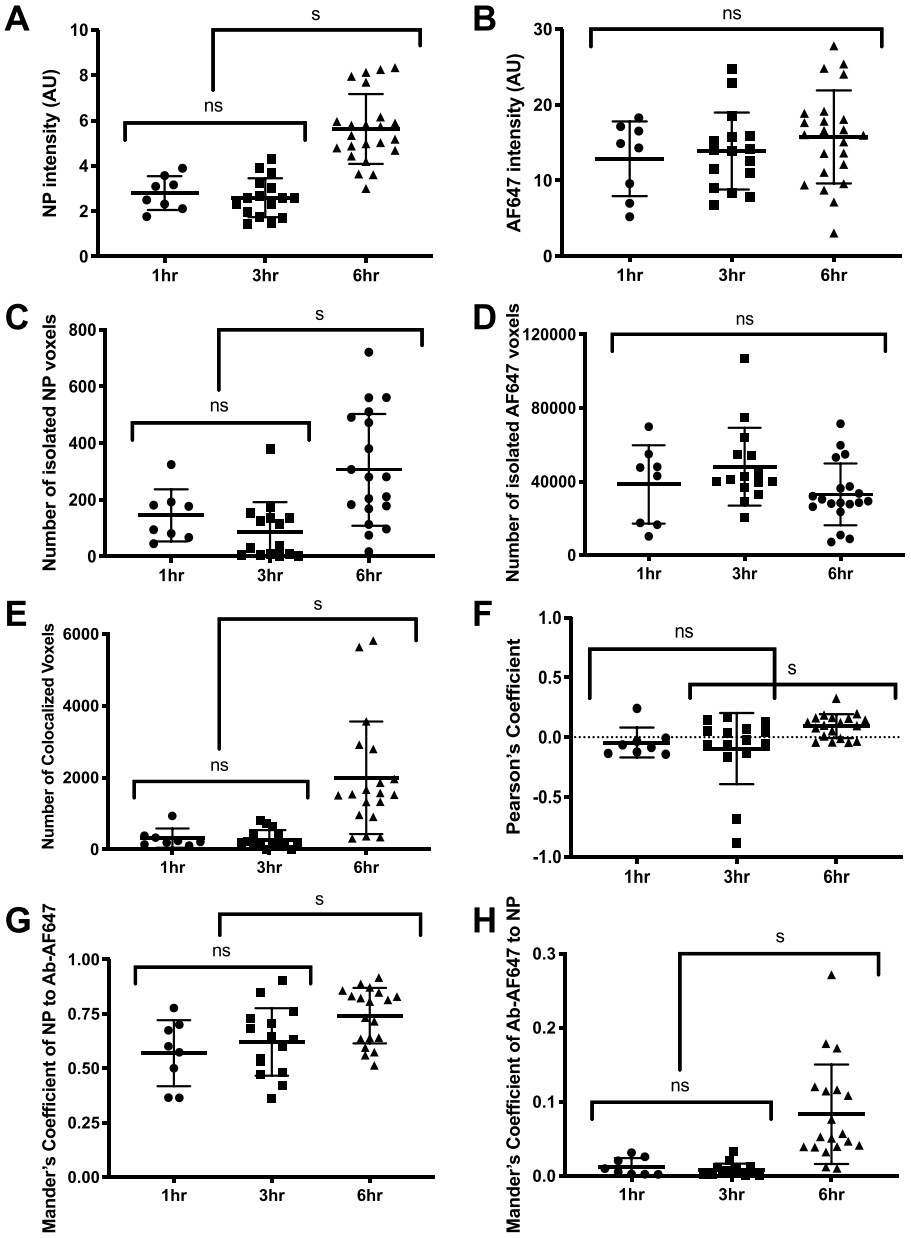

Figure 4. Image analysis of two-photon microscopy images of 5 nm aEGFR-AuNPs in A431 cells. (A) Distribution of mean intensities of AuNP luminescence and (B) of antibody fluorescence from labeled cells at different time points. (C) Scatterplots of voxels with either AuNP luminescence or (D) antibody fluorescence that are not colocalized with each other inside labeled cells. (E) The number of colocalized voxels containing both the antibody fluorescence and the AuNP luminescence. (F) Pearson's correlation coefficient between AuNP luminescence and antibody fluorescence in voxels with colocalized signals. (G) Mander's colocalization coefficients for AuNP luminescence. Note that after 1 h incubation of cancer cells with 5 nm aEGFR-AuNPs, ∼65% of AuNP luminescence was colocalized with antibody fluorescence, and this fraction increased to ∼84% after 6 h incubation. (H) Mander's colocalization coefficients for antibody fluorescence. Fluorescence from antibodies was marginally colocalized with AuNP luminescence with MCCs increasing from just ∼1% after 1 h to ∼6% after 6 h of incubation. Labels "ns" and "s" denote values that are statistically "not significant" and "significant", respectively (p-value < 0.05). Each data point in the plots represents an individual cell.

where each point indicates antibody fluorescence and AuNP luminescence values of an imaging voxel (Figure 3B). As can be seen in the example in Figure 3B, there is a significant increase in the number of voxels with a strong AuNP luminescence at the 6 h time point relative to 1 and 3 h. Further, it is evident that a substantial number of voxels with a high AF647 fluorescence signal do not coexhibit a strong TPL from AuNPs, while some voxels with strong nanoparticle luminescence have a negligible AF647 fluorescence. Quantitative analyses of these signal intensity data, including colocalization coefficients, are shown in Figure 4.

There was no significant increase in either intensity or the number of voxels with antibody fluorescence signal per labeled cell over time (Figure 4B and D) that could be due to a balance between antibody uptake and exocytosis. In contrast, there was a significant increase in the TPL signal from AuNP aggregates in individual cells after 6 h of incubation (Figure 4A). This increase was due to both the increased number of voxels with AuNP luminescence (Figure 4C and E) and the

https://doi.org/10.1021/acsnano.0c08128
ACS Nano 2021, 15, 9495−9508

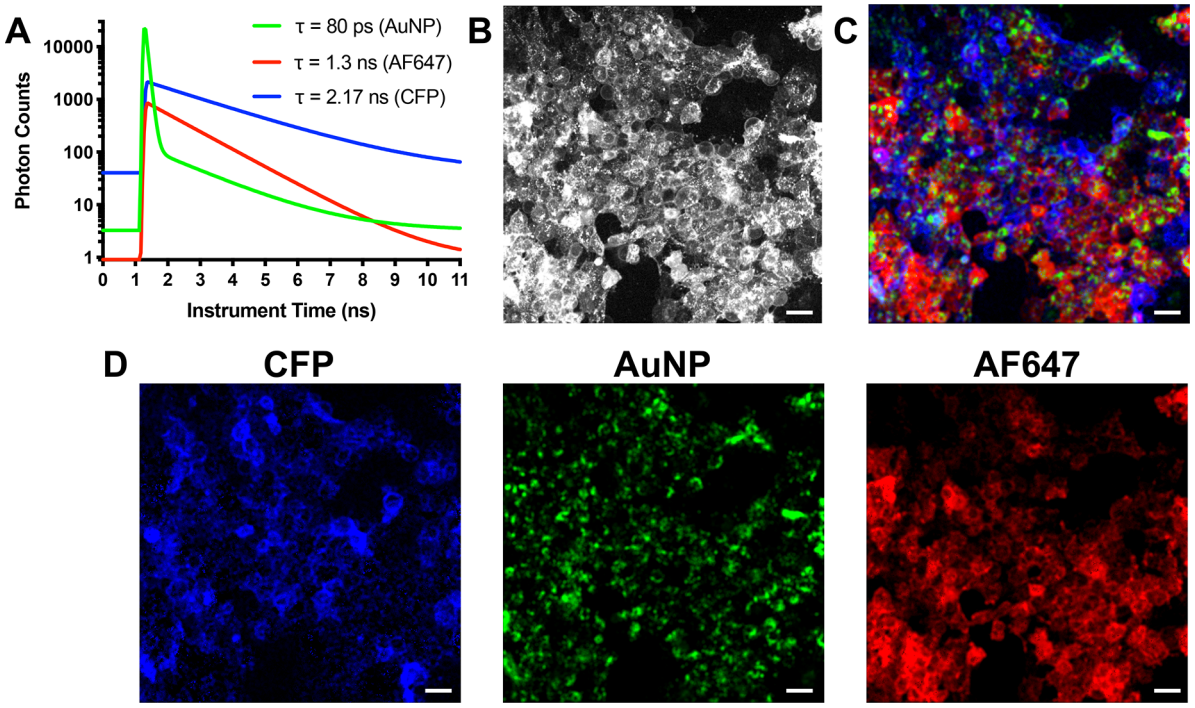

Figure 5. FLIM of 5 nm aEGFR-AuNPs in A431 cells. (A) Fluorescence lifetime curves obtained from (i) intracellular 5 nm aEGFR-AuNPs conjugated with unlabeled anti-EGFR antibodies (green); (ii) cells incubated with AF647-labeled anti-EGFR antibodies (red); and CFP that was used for cell plasma membrane labeling. Note that the lifetime of each fluorescence component was measured without the presence of any other components. (B) FLIM intensity and (C) FLIM with three lifetime components corresponding to gold cores (green), AF647-labeled antibodies (red), and cell membrane CFP (blue) after incubation of CFP-transfected A431 cells with 5 nm aEGFR-AuNPs prepared using AF647-labeled anti-EGFR antibodies. (D) FLIM of each individual component shown in (C). Cells were incubated for 24 h in all experiments. Scale bars are 20 μm.

greater number of voxels with a relatively high AuNP luminescence (Figure 3B). Considering that TPL of AuNPs is greatly enhanced with an increase in cluster size,[56] this observation is consistent with an increase in the number of nanoparticle clusters in a cell and the formation of clusters with larger sizes. It is noteworthy that, on average, there were at least ~17-fold more voxels with antibody fluorescence than with AuNP luminescence. The relative abundance of voxels with antibody-only fluorescence indicates that the formation of clusters of AuNPs is a rare event. Previously, an enhancement factor of ~40-fold similar to the one in our study was observed in clusters of 21 nm spherical AuNPs separated by ~6.1 nm edge-to-edge.[54] TPL enhancement increases with an increase in strength of the plasmon resonance coupling between spherical nanoparticles, which in turn scales as $(d/D)^{-3}$ for pairs of AuNPs smaller than 80 nm diameter, where d is the center-to-center distance between particles and D is the particle's diameter.[57−59] Therefore, a pair of 5 nm diameter AuNPs would have a similar plasmon resonance coupling strength at ~1.5 nm edge-to-edge distance as a pair of 21 nm AuNPs at the 6.1 nm separation. It is important to note that this estimate is not intended to extrapolate the separation between 5 nm AuNPs in our cell study; it is only an illustration of relative changes in the strength of plasmon resonance coupling with the core size. Indeed, the effect of plasmon coupling also depends on the number of nanoparticles in a cluster,[55] which complicates estimations of AuNP separation solely based on a TPL enhancement factor.

Unexpectedly, a significant number of voxels with AuNP luminescence was not colocalized with antibody fluorescence, indicating spatial separation of gold cores from antibody coating inside cells (Figure 4C). The total number of isolated AuNPs increased after 6 h of incubation (Figure 4C). However, Mander's colocalization coefficients (MCCs) for the AuNP luminescence *versus* antibody fluorescence changed from ~65% at 1 and 3 h to ~84% at 6 h, indicating that there was a significant decrease in the relative average amount of isolated AuNP luminescence voxels per cell (Figure 4G; Supplementary Figure 4). Interestingly, MCCs showed only marginal colocalization of antibody fluorescence signal with TPL of gold cores (Figure 4H). This result suggests a relatively rare occurrence of AuNP clustering and a dominant number of voxels with antibody fluorescence compared to ones with TPL of gold cores, as discussed above. Pearson's correlation coefficient was used to evaluate the correlation between the intensity of AuNP luminescence and antibody fluorescence in voxels with colocalized signals. The coefficient was close to 0 for all time points, indicating a lack of a linear correlation between TPL from 5 nm AuNPs and antibody fluorescence (Figure 4F). This result is likely due to a nonlinear effect of nanoparticle aggregation on their luminescence intensity.

Fluorescence Lifetime Imaging of Cells Labeled with 5 nm aEGFR-AuNPs. TPL of AuNPs is characterized by very short, almost instantaneous lifetimes (<1 ns).[60,61] This fundamental property can be used to distinguish this type of luminescence from fluorescence, whose lifetimes are typically much greater than 1 ns. Lifetime-based imaging microscopy, often somewhat narrowly referred to as fluorescence lifetime imaging microscopy, or FLIM, is used to generate different image contrasts by measuring light emission lifetimes in response to pulsed illumination for each image voxel. This imaging modality is highly advantageous by effectively

https://doi.org/10.1021/acsnano.0c08128
ACS Nano 2021, 15, 9495−9508

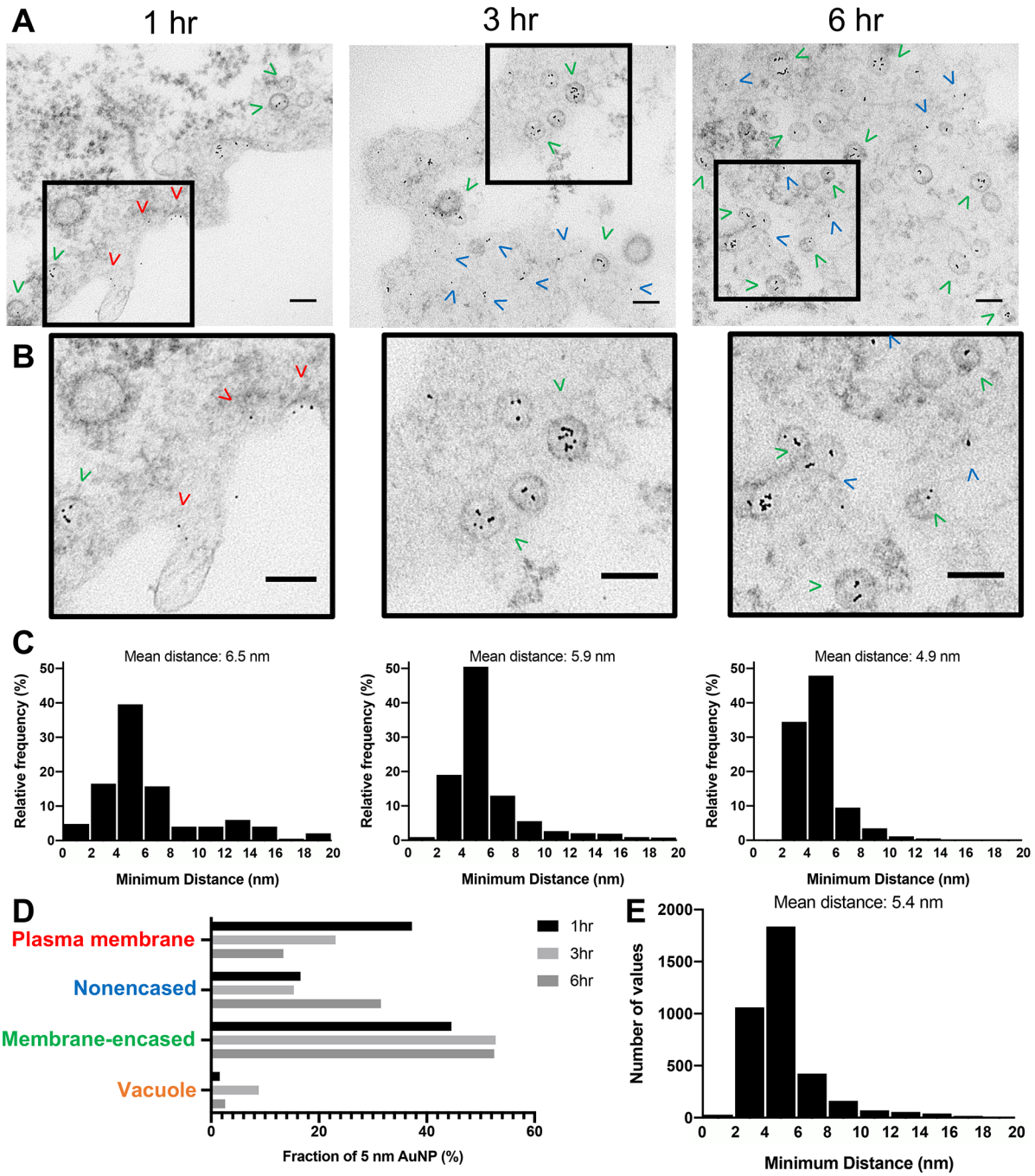

Figure 6. Transmission electron microscopy (TEM) of A431 cell labeled with 5 nm aEGFR-AuNPs. The cells were incubated with the nanoparticles for 1, 3, and 6 h, respectively. (A, B) TEM images at 1, 3, 6 h time points. Scale bars are 100 nm. The colors of arrows correspond to various cellular compartments shown in (D). (C) Histograms of interparticle center-to-center distances at each time point. (D) Subcellular localization of 5 nm AuNPs at different time points from TEM images. (E) Histogram of minimum interparticle distances summarizing TEM data from all time points obtained from 48 TEM images.

separating the short-lived luminescence from any fluorescence components including in a situation of spectral overlap. Here, we carried out an initial evaluation of FLIM in monitoring gold cores and antibody coating of 5 nm aEGFR-AuNPs following their uptake by cancer cells. First, TP fluorescence lifetime curves were measured for three entities: (1) cancer cells labeled with EGFR-targeted 5 nm AuNPs conjugated with unlabeled anti-EGFR antibodies; (2) cells incubated with AF647-labeled anti-EGFR antibodies (AF647-Ab) alone; and (3) cells that were transfected to express CFP on their membranes (Figure 5A and Supplementary Figure 4). The lifetime measurements were carried out in cells rather than in suspension to better account for any potential influence of the intracellular environment. The TPL of intracellular 5 nm AuNPs was characterized by a double-exponential decay with a major (99.7% amplitude) very short lifetime component of ~80 ps and a minor (~0.27% amplitude) longer lifetime component of ~1.6 ns. Previous analyses of TP fluorescence lifetime of gelatin-coated ~80 nm spherical AuNPs, gold nanorods (AuNRs), and gold triangles inside ovarian cancer

https://doi.org/10.1021/acsnano.0c08128
ACS Nano 2021, 15, 9495−9508

cells revealed a single-decay photoluminescence with a time constant of ≤100 ps.[61] A similar decay constant was obtained for CTAB-coated AuNRs in canine kidney cells.[60] On the other hand, a much slower decay constant of ∼1.0 ns was observed in large gold nanorods with a long axis of up to 540 nm.[62] This report also stated that the TP fluorescence decay can vary from 0.8 to 2 ns depending on the size and shape of AuNPs. In general, the effect of TPL of AuNPs is attributed to a combination of recombination processes between excited electrons in the sp-band and holes in the d-band.[49] It was hypothesized that the long lifetime component is associated with excited electrons located near the Fermi level.[62] However, a correlation between specific gold nanostructures and their luminescence lifetime has not been clearly established. It is conceivable that the double-exponential decay curve of 5 nm AuNPs reflects heterogeneous clustering of nanoparticles inside cells. AF647-Abs and CFP signals were characterized by single-exponential decays with lifetime components of 1.3 and 2.17 ns, respectively, that is, at least 16-fold longer than the fast decay component of 5 nm AuNPs.

Next, we evaluated the feasibility of using lifetimes to image the intracellular distribution of AuNP core aggregates (τ = 80 ps) and AF647-labeled antibody (τ = 1.3 ns) in the context of cell morphology labeled by CFP fluorescence (τ = 2.17 ns) (Figure 5). An example of a total intensity-based image of femtosecond pulse-excited emission spanning the wavelengths of 5 nm AuNP TPL and CFP and antibody-AF647 fluorescence is shown in Figure 5B. Using the three mean lifetime constants obtained from signal decay analysis in the previous step, the total intensity image was clearly separated into three images corresponding to the cell membrane (CFP), gold cores, and AF647-antibodies (Figure 5C, D). Closer inspection of these images revealed that the spatial distribution patterns of AuNPs and antibodies inside cells were not identical, and, in fact, they were quite different. It was evident that some cell regions contained predominantly either gold cores or the antibody; this result agrees with the TPL imaging discussed above. Interestingly, multiple cells exhibited a doughnut-like pattern where antibodies surround a central region with the predominant signal from gold cores (Figure 5C). These results indicate that 2P-FLIM is a powerful technique to analyze the fates of hybrid gold nanostructure components, *e.g.*, the gold cores and attached antibodies, in living cells.

TEM of 5 nm aEGFR-AuNPs in Cells. TPL imaging showed clustering of 5 nm aEGFR-AuNPs inside cancer cells. To gain more detailed and independent information about the specific location of gold cores and their spacing, we imaged the specimens using TEM.

Cancer cells were incubated with 5 nm aEGFR-AuNPs for 1, 3, and 6 h to allow nanoparticle endocytosis and trafficking inside the cells (Figure 6A and B and Supplementary Figure 6). Fixed specimens were counterstained such that TEM images revealed both the gold densities and intracellular structures. We found the nanoparticles predominantly in four intracellular locations: the plasma membrane, membrane-encased intracellular vesicles, cytosol (nonencased), and a small subset of vacuole-like structures (Figure 6D). At the 1 h incubation time point, more than 44% of the particles were located in "membrane-encased" vesicles, and ∼37% were located on the "plasma membrane", which is consistent with a typical receptor-mediated uptake.[37,55] At later time points (3 and 6 h), gold particles were found mostly in endocytic structures (∼52% at 3 and 6 h) with a decreased fraction (∼23 and ∼13% particles at 3 and 6 h, respectively) associated with the plasma membrane. In addition, we observed a small fraction of nanoparticles ranging from ∼1.5% to 8.8% in vacuoles that might indicate early stages of autophagy due to nanoparticle-induced stress.[63]

Unexpectedly, ∼15% (1 and 3 h) and ∼31% (6 h) of gold particles were located outside of any membrane-encased organelles. Since 5 nm aEGFR-AuNPs are too big to be translocated directly through the plasma membrane, we hypothesized that these nanoparticles entered the cytosol through an endosome disruption mechanism. Endosomal rupture by the "proton sponge effect" has been used for cytosol delivery in several nanoparticle formulations.[64] Usually, nanoparticle coatings enriched in cationic groups are used for this purpose, such as peptides with positively charged lysine and arginine side chains.[65] However, the introduction of histidine residues with a pK_3 of just 6.0 was also shown to significantly increase the cytosol delivery through the proton sponge effect.[66,67] It was also reported that the pK_3 of citrate molecules is 6.4, comparable to histidine.[68] Previously, we showed that 5 nm aEGFR-AuNPs have a negative zeta-potential of ∼47 mV at neutral pH,[41] which indicates a high residual amount of citrate ions on the nanoparticle surface. These ions could have sufficiently high buffering capacity similar to histidine side chains, thus inducing endosomal escape of gold nanoparticles. Also, an increase in osmotic pressure inside an endosome associated with encapsulation of AuNPs and antibodies could further increase the destabilization of the endosomal membrane due to influx of equilibrium restoring water molecules. If the antibody coating is detached from 5 nm aEGFR-AuNPs inside endosomes, the cytosol fraction of AuNPs is likely responsible for the spatial separation of gold cores and antibodies that was observed by TPM, as discussed above. Indeed, after endosomal uptake both the gold cores and the antibodies are located in the same spatial confinement where they are transported together to late endosomes and, then, to lysosomes during the time frame of our observations. Regular TPM does not have sufficient resolution to separate signals from AuNPs and antibodies inside these intracellular compartments. Below, we provide arguments supporting the intracellular detachment of antibodies from gold cores.

Based on TEM analysis (Figure 6E), AuNPs tended to be closely spaced on average by a ∼5.4 nm center-to-center distance, which corresponds to ∼0.4 nm side-by-side separation with ∼54% of the particles in even closer proximity. This separation is substantially closer than the hydrodynamic diameter (∼22 nm) of the 5 nm aEGFR-AuNPs. Furthermore, virtually all AuNPs in closely spaced clusters were separated by distances smaller than the hydrodynamic diameter of their antibody conjugates (Figure 6E). These data suggest that nanoparticles were not sterically hindered by conjugated antibodies, likely due to the antibody coating degradation. However, it is also important to note that the distances measured from TEM are subject to artifacts.[69] Perhaps the most significant one in our studies could be due to the thickness of TEM slices being 70 nm; therefore, some particles can overlay on top of each other, which could create a perception of a closer spacing. This artifact is most likely responsible for some center-to-center distances being less than the nanoparticle's diameter.

https://doi.org/10.1021/acsnano.0c08128
ACS Nano 2021, 15, 9495−9508

Antibodies were conjugated to 5 nm aEGFR-AuNPs through a thiol−gold bond that has a ∼4.6 nM dissociation constant.[41] Therefore, a potential antibody displacement mechanism from gold cores is by a ligand exchange reaction with other thiol-containing molecules.[38,70] For example, GSH is a tripeptide with a thiol group from a cysteine residue that is present at the concentration of 5 mM inside mammalian cells.[71] To evaluate the possibility of antibody becoming separated from the gold surface by ligand exchange with GSH, we took advantage of the effect of AF647 fluorescence quenching in the proximity of the gold surface. In particular, we measured the intensity of AF647 fluorescence in a cuvette containing 5 nm aEGFR-AuNPs before and after adding GSH. Dithiothreitol (DTT) at a high concentration of 10 mM was used as a positive control because of its well-known ability to displace thiolated molecules from gold surfaces.[38,72,73] We found that GSH at a 0.65 mM concentration was almost as efficient as DTT in displacing fluorescently labeled antibodies from AuNPs (Figure 7). This experiment confirmed the feasibility of biodegradation of the dithiol-bound antibody coating of 5 nm aEGFR-AuNPs by intracellular thiols such as GSH, likely within minutes of cellular uptake. The antibody displacement reached a plateau after ∼60 min with an overall displacement efficiency of ∼87%. Furthermore, we showed by UV−vis spectrophotometry, DLS measurements, and TEM that displacement of antibodies leads to aggregation of AuNPs (Supplementary Figure 7). Interestingly, all methods indicate the formation of larger aggregates after incubation with DTT. It is consistent with our previous observation that a GSH layer on gold nanoparticles can provide some protection from irreversible aggregation.[74]

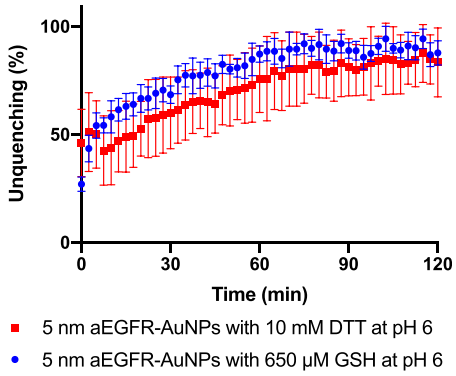

Figure 7. Changes in fluorescence of 5 nm aEGFR-AuNPs conjugated with Alexa Fluor 647-labeled antibodies after the addition of either glutathione (GSH) or dithiothreitol (DTT) at pH 6 (mean ± SD, N = 3). The percentage scale on the y-axis corresponds to changes in fluorescence intensity between the 5 nm aEGFR-AuNPs and a mixture of free 5 nm AuNPs and free AF647-labeled antibodies at concentrations matching their concentrations in the 5 nm aEGFR-AuNP conjugates; therefore, the 100% unquenching corresponds to the complete displacement of antibodies from the nanoparticle conjugates.

In addition, it is important to note that the proteolytic activity of endosomal proteases can also contribute to the nanoparticle's coating biodegradation. Previously, a model system consisting of gold nanoparticles coated with dye-quenched ovalbumin (Au@Ova-DQ) was developed to probe the proteolytic activity of cellular endosomes.[75] Au@Ova-DQ nanoparticles exhibited a time-dependent fluorescence signal increase following uptake by 3T3 fibroblasts, indicating proteolysis of the coating with the initial fluorescence signal visible ∼1 h after cell treatment with the nanoparticles. Therefore, proteolysis of antibodies is also likely to be involved in the biodegradation of 5 nm aEGFR-AuNPs.

CONCLUSIONS

In this study, we observed a strong TPL from cancer cells labeled with anti-EGFR antibody-conjugated ultrasmall spherical AuNPs (5 nm aEGFR-AuNPs). Using TP excitation fingerprinting, we showed that this photoluminescence signal is associated with the intracellular formation of clusters of 5 nm AuNPs that exhibited ∼40-fold brighter TPL than unclustered (colloidal) 5 nm AuNPs. We used this effect of 5 nm AuNPs clustering-associated TPL enhancement to study the intracellular fates of both the anti-EGFR antibody coating and the gold cores of 5 nm aEGFR-AuNPs after cellular uptake of these hybrid nanoparticles by cancer cells. Our data from TPM, FLIM, TEM, and *in vitro* assays suggest the following sequence of events (Figure 8). After receptor-mediated endocytosis, antibodies conjugated to 5 nm aEGFR-AuNPs undergo thiol-mediated dissociation that releases the 5 nm gold cores into the lumen of endosomes, where the individual nanoparticles begin forming clusters with a strong TPL. Since the AuNPs lose steric stabilization due to the biodegradation of their coating, the aggregation is likely driven by ions present at physiological concentrations that are sufficiently high to reduce any residual electric double layer on the nanoparticles' surface. The number of voxels in TPM images with strong luminescence from AuNPs remained the same at 1 and 3 h

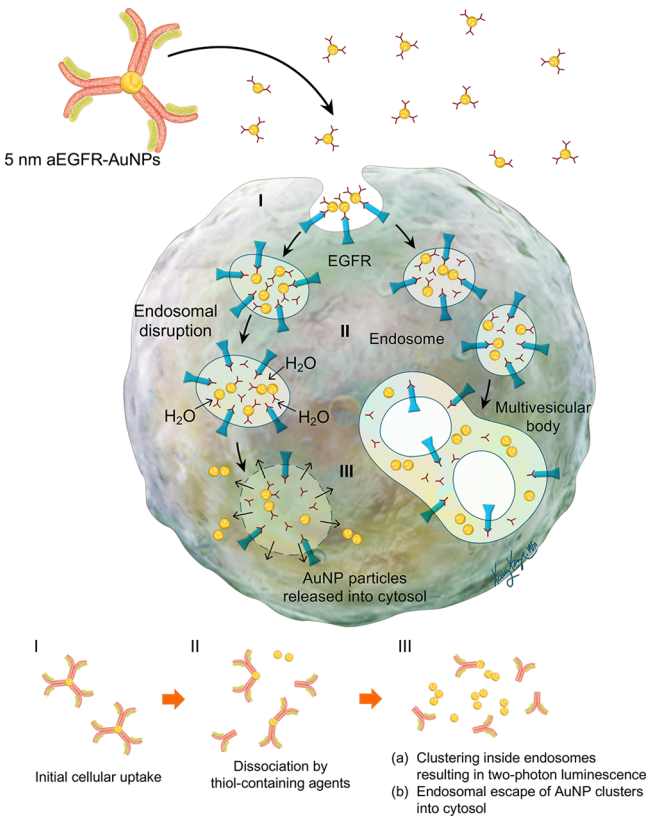

Figure 8. Schematic presentation of 5 nm aEGFR-AuNPs' fate inside cells.

https://doi.org/10.1021/acsnano.0c08128
ACS Nano 2021, 15, 9495−9508

time points, and it significantly increased at the 6 h time point (Figures 3 and 4). We hypothesize that the increase in TPL of AuNPs at 6 h is due to progressive accumulation of AuNPs in late endosomes, which increases their local concentration and, therefore, probability of aggregation. In addition, it is conceivable that physisorption of intracellular proteins might render temporary colloidal stability to AuNPs following the biodegradation of their antibody coating; this possibility was previously demonstrated.[76] A decrease in this stabilization at 6 h might contribute to the increase in the number of nanoparticle aggregates at this time point. TEM analyses revealed the presence of AuNPs outside of any membrane-encased intracellular organelles, which indicated the endosomal escape of AuNPs (Figure 6). This escape could be triggered by the buffering capacity of residual citrate molecules on the surface of AuNPs, which have a sufficiently high p*K* to induce the proton sponge effect of endosomal disruption. The disruption of endosomal membranes would allow clusters of AuNPs to escape into the cytosol. These escaped clusters could be associated with the optically resolved spatial separation of TPL signals from fluorescently labeled antibodies and 5 nm AuNPs (Figures 3 and 4). Approximately 35% of voxels with AuNP luminescence were not colocalized with antibody fluorescence at 1 and 3 h time points, with this number being ~16% at 6 h, indicating spatial separation of AuNP cores and antibodies inside cells (Figures 3 and 4). This observation was also confirmed by 2P-FLIM (Figure 5).

In our studies, TPL of AuNPs does not detect the initial antibody detachment from the nanoparticles inside cells; it shows the downstream consequence of the antibody layer degradation−nanoparticle aggregation. Therefore, we cannot unequivocally say if an antibody fluorescent signal is associated with already detached or nanoparticle-bound antibodies. However, TPL provides a useful tool to monitor the loss of colloidal stability of AuNPs inside cells due to coating biodegradation and to determine the spatiotemporal distribution of intracellularly formed nanoparticle clusters. The latter led to an unexpected observation of an optically resolved spatial separation of gold nanoclusters and fluorescently labeled antibody coating. Furthermore, our data presented in Figure 7 indicate that the initial coating degradation step could potentially be detected using nanoparticle tracking imaging techniques where detection of fluorescence intensity changes (*i.e.*, increase in fluorescence during detachment of antibodies) can be detected if a gold nanoparticle is tracked during imaging. Note that these results have been obtained in one cell line. The observed trends need to be further validated in other cell lines targeted with various antibody-conjugated nanoparticles.

The current study demonstrates that TPM and FLIM can be powerful tools for monitoring the intracellular behavior of hybrid AuNPs under development for imaging and therapeutic applications. In particular, cells labeled with 5 nm aEGFR-AuNPs could be detected with high contrast *in vivo* (Supplementary Figure 8). Considering a high photostability of spherical AuNP clusters under pulsed laser irradiation,[76] TPM can be useful for a longitudinal monitoring of AuNP-labeled cells *in vivo*.

MATERIALS AND METHODS

Synthesis of 5 nm Gold Nanoparticle Antibody Conjugates. Citrate-coated spherical 5 nm AuNPs were received from NanoHybrids (Austin, TX, USA) as a gift. Monoclonal anti-EGFR clone 225 (Sigma, E2156) was used as a targeting antibody. Antibody conjugation was carried out following a protocol previously developed by us that consists of four main steps: (1) mild oxidation of the antibody's carbohydrate moiety to form functional aldehyde groups; (2) the antibody's fluorescent labeling through amine groups; (3) attachment of a bifunctional hydrazide-PEG-dithiol linker to the fluorescently labeled antibody's aldehyde group; and, finally, (4) conjugation with AuNPs through the linker's dithiol group.[46] In this sequence, the formation of aldehyde groups precedes the antibody's fluorescent labeling to prevent potential oxidation of the fluorophores. Briefly, an antibody solution received from the manufacturer was filtered through a 100 kDa MWCO centrifuge filter (EMD Millipore). The purified antibodies were collected from the filter using 100 mM sodium phosphate buffer, pH 7.5. Then, 100 μL of 100 mM sodium periodate (Sigma) was added to 1 mL of 1 mg/mL antibody solution, and the mixture was kept on a shaker at 350 rpm at room temperature (RT) for 30 min in the dark. During this step, the antibody's carbohydrate moiety undergoes mild oxidation to form aldehyde functional groups. The reaction was stopped by the addition of a 50-fold volume excess of PBS. The activated antibody was washed and concentrated by centrifugation through a 10 kDa MWCO centrifuge filter (EMD Millipore) for 20 min at 3100*g* at 4 °C. The activated antibody was then labeled (on amine groups) with Alexa Fluor 647 (AF647) dye succinimidyl ester (A20173, Invitrogen) following the manufacturer's protocol. A 100 μL amount of fluorescently labeled antibodies at 1 mg/mL in PBS buffer, pH 7.5, was mixed with 4 μL of 23.25 mM (~150-fold molar excess) of the bifunctional hydrazide-PEG-dithiol linker (dithiolalkane aromatic-PEG$_6$-NHNH$_2$, SPT-0014B, SensoPath Technologies), and the mixture was incubated in the dark for 1 h at RT on a shaker at 350 rpm. Unreacted linker molecules were removed by a 10 kDa MWCO filter centrifugation at 3100*g* for 20 min at 4 °C, and the linker−antibody conjugates were reconstituted at 100 μg/mL in PBS. The antibody−linker solution at 100 μg/mL in PBS was added to 5 nm AuNPs at an optical density (OD) = 1, to achieve final antibody concentrations of 47 μg/mL, corresponding to ~5-fold molar excesses of antibodies. The suspension was incubated in the dark for 1 h at RT on a shaker at 350 rpm. Then, 5 kDa mPEG-SH (MPEG-SH-5000, Laysan Bio) at 0.05 mg/mL in PBS was added to the suspension to achieve the final concentration of 3.8 μg/mL, followed by an additional 30 min incubation at RT on a shaker at 350 rpm. Then, antibody and PEG-conjugated 5 nm AuNPs were sedimented by ultracentrifugation at 100000*g* for 1 h at 4 °C. The final antibody-conjugated nanoparticles were resuspended in PBS at an OD ≈ 1.5 and stored at 4 °C for a future experiment. UV−vis spectrophotometry (Synergy HT, BioTek Instruments), dynamic light scattering (DLS) (Zetasizer Nano, Malvern), and zeta-potential analysis (DelsaNano C, Beckman Coulter) were used to characterize spectral properties, size, and surface charge of the nanoparticles, respectively.

***In Vitro* Aggregation of 5 nm AuNPs and AuNP−Antibody Conjugates.** Citrate-coated 5 nm AuNPs were aggregated using benzylmercaptan.[77] Note that benzylmercaptan requires handling in an air-circulating fume hood. AuNPs at OD = 1 were mixed with either 12.5 or 25 μM benzylmercaptan at a 1:1 v/v ratio and were incubated for 30 min at RT on a shaker at 350 rpm. Aggregation of AuNP−antibody conjugates was triggered by the addition of a ~1000-fold molar excess of 1 kDa NHS-PEG-NHS (NanoCS) to the conjugates for 30 min at RT and 24 h at 4 °C. The absorbance spectra of the aggregated samples were measured using UV−vis spectrophotometry (Synergy HT, BioTek Instruments). Then, 79.5 μL aliquots of the samples were mixed with 69 μL of 10.76 mg/mL collagen and 1.5 μL of 1 M NaOH. The mixtures were loaded into Lab-Tek II 8-well chambered coverglass (Nalge Nunc International), and the gels were allowed to solidify at 37 °C for 20 min before TP imaging. Excitation spectra of the aggregated nanoparticles were measured from 740 to 990 nm in 10 nm increments stepped manually using the Mai Tai control software (Spectra Physics, Mountain View, CA, USA) with the emission detected using a Leica nondescanned detector with a 560−680 nm bandpass emission filter (see the full system description below). Emission spectra were measured from 400 to

https://doi.org/10.1021/acsnano.0c08128
ACS Nano 2021, 15, 9495−9508

730 nm with 830 and 880 nm excitation wavelengths, using the descanned optical path of the Leica SP5MP confocal spectral scanner.

Two-Photon Microscopy Imaging. EGFR-positive A431 cells (human epidermoid carcinoma) were cultured in HyClone DMEM/high glucose (GE Healthcare Life Sciences) media supplemented with 10% FBS and 1% PS penicillin−streptomycin (Life Technologies) in a humidified atmosphere and 5% CO_2 at 37 °C. Cells were seeded in a Nunc glass base dish (Thermo Fisher Scientific, 150682, 27 mm) at 500 000 cells/well. The cell membrane was stained with CellLight plasma membrane-CFP, BacMam 2.0 (Molecular Probes) according to the manufacturer's instruction. Then, 5 nm aEGFR-AuNPs were added to cells at a final concentration of 2.36 μg/mL and incubated at 37 °C. After incubation, cells were washed with warm PBS containing Ca^{2+} and Mg^{2+} to remove free nanoparticles before cell collection using trypsinization. Cells were collected by centrifugation at 300*g* for 10 min. The cell pellets were reconstituted in 100 μL of 4% paraformaldehyde (Electron Microscopy System) in PBS. Then, 79.5 μL of fixed cells was added to 69 μL of 10.76 mg/mL collagen mixed with 1.5 μL of 1 M NaOH. The mixtures were added to Lab-Tek II eight-well chambered coverglass (Nalge Nunc International) and incubated at 37 °C for 20 min to form a collagen gel. TP imaging was performed using a Leica TCS SP5MP/DMI6000-based laser scanning microscope system (Leica Microsystems). The system included two Mai Tai titanium sapphire femtosecond-pulsed lasers (Spectra Physics), two electro-optical modulators (EOM, Linos), custom polarization-based merge optics, and a 25× NA 1.1 water immersion objective (Nikon). The emitted light was detected using a four-channel nondescanned detector (Leica) consisting of two photo-multiplier tube detectors and two hybrid avalanche photodiode photomultiplier tube detectors (HyD) optically arranged with appropriate dichroic mirrors and bandpass filters (450−500, 500−520, 518−558, and 560−680 nm, Semrock). Excitation at 830 nm was used for most image capture except for excitation scanning. Some spectral emission overlap exists between CFP, AuNP, and AF647 signals depending on each channel wavelength bandpass and detector amplification settings. The spectral bleed through, typically ∼33% (CFP to AuNP channel) and 34% (AuNP to CFP channel), was removed by linear unmixing using the Dye Separation function in the LAS software. For quantitative analysis of cell images, intensity-based thresholds were applied at 10% and 4% of the maximum intensity of the AuNP luminescence and AF647 fluorescence, respectively. The degree of colocalization was analyzed using the colocalization function in Imaris software (Bitplane) in terms of the Pearson's or Mander's coefficients.

Using constant microscope illumination and detection settings, the brightness of TPL of colloidal 5 nm aEGFR-AuNPs and intracellular 5 nm aEGFR-AuNPs was determined as the average pixel intensity in the regions of interest segmented at 10% of the maximum intensity threshold. The TPL brightness values obtained from intracellular 5 nm aEGFR-AuNPs were divided by the intensity of the colloidal 5 nm aEGFR-AuNPs to determine the relative signal intensity.

Two-Photon FLIM Setup. Two-photon excited lifetime imaging was performed using the same Leica SP5 TCS system as above, by laser gating and time-correlated single-photon counting managed by the SPC-150/DP-120 lifetime imaging subsystem (Becker & Hickl). The 1 femtosecond laser was tuned to 830 nm with ∼1.4 W infrared power at the laser output, and the beam intensity was decreased to 12.5% or 25% by a neutral density filter and passed through one EOM and dual-stacked broadband polarizers. Infrared power at the objective back aperture was in the 25−55 mW range. Time-correlated single photon counting was performed with bidirectional scanning in 512 × 512 or 1024 × 1024 formats (2.42 or 1.21 μm pixel size at zoom setting 1, respectively). Lifetime images were generated using the SPCImage software (Becker & Hickl). Characteristic lifetimes of each component—5 nm AuNPs, AF647, and CFP—were determined using control samples, respectively: (1) cells incubated for 24 h with 5 nm AuNPs conjugated with unlabeled aEGFR antibodies; (2) cells incubated for 24 h with aEGFR-AF647 antibodies; and (3) cells expressing CFP on their membranes.

For experimental specimens, images of component lifetime amplitudes were calculated, on a pixel-by-pixel basis, by curve fitting to double- or triple-exponent models:

$$T_{m,i} = \sum_i a_i T_i \text{ with } \sum_i a_i = 1$$

where a_i= amplitude of the lifetime components.

TEM Preparation and Analysis. Cells labeled with 5 nm aEGFR-AuNPs were fixed with a solution containing 3% glutaraldehyde and 2% paraformaldehyde in 0.1 M cacodylate buffer, pH 7.3. Then, the samples were washed in 0.1 M sodium cacodylate buffer and treated with 0.1% Millipore-filtered cacodylate-buffered tannic acid, followed by treatment with 1% buffered osmium and staining en bloc with 1% Millipore-filtered uranyl acetate. The fixed, stained samples were dehydrated in increasing concentrations of ethanol and embedded in LX-112 medium. The resin was polymerized in a 60 °C oven for approximately 3 days. Ultrathin sections were cut using a Leica Ultracut microtome (Leica, Deerfield, IL, USA), stained with uranyl acetate and lead citrate in a Leica EM stainer, and examined in a JEM 1010 transmission electron microscope (JEOL, USA, Inc., Peabody, MA, USA) at an accelerating voltage of 80 kV. Digital images were obtained using the AMT imaging system (Advanced Microscopy Techniques Corp, Danvers, MA, USA). Nanoparticles in 48 TEM images were manually counted (2866 AuNPs in total) to categorize the cellular location based on organelles' morphological features. Nanoparticles in vesicles, including endosomes and lysosomes, were called "membrane-encased". Particles located in the cytosol away from any membranous structures were classified as "nonencased". Particles closely located in the plasma membrane without being encased in a subcellular membrane were categorized as having a "plasma membrane" localization. Particles were assigned to be in a "vacuole" if a membrane-encased organelle was bigger than 500 nm in diameter and had no submembrane organelles inside. To estimate center-to-center distances between particles, particles from TEM images were outlined using the spots function in IMARIS (Bitplane). Then, interparticle distances were plotted as a histogram.

Fluorescence Measurements of 5 nm aEGFR-AuNPs Incubated with GSH and DTT. Samples of 5 nm aEGFR-AuNPs conjugated with AF647-labeled antibodies were prepared at OD = 0.906 of the plasmonic peak of AuNP cores, corresponding to 95.3 nM of AuNPs. The concentration of gold nanoparticles was determined using their optical density.[78] Nanoparticle conjugates were mixed with glutathione (Thermo Fisher Scientific) and dithiothreitol (Thermo Fisher Scientific) at pH 6 in PBS at a concentration of 650 μM and 10 mM, respectively. AF647 fluorescence was recorded immediately after addition of GSH or DTT every 2.5 min over 120 min using a Synergy HT microplate reader (BioTek Instruments, Winooski, VT, USA). AF647-labeled antibodies without conjugating linker were mixed with PEGylated 5 nm AuNPs at 2.7 molar excess at pH 6 in PBS to create a control representing complete displacement of labeled antibodies from the gold nanoparticles; the antibody molar excess was based on the average number of antibodies attached to the particles in 5 nm aEGFR-AuNP conjugates. AF647 fluorescence of the control was measured over time using the same conditions as for the GSH and DTT mixtures with 5 nm aEGFR-AuNPs to account for fluorescence quenching. Fluorescence changes were indicated as unquenching using the following equation:

$$\text{Unquenching (\%)} = \left(\frac{F_{t,a} - F_{t,0}}{F_{t,b} - F_{t,0}}\right) \times 100$$

where $F_{t,a}$ is the fluorescence of 5 nm aEGFR-AuNPs mixed with GSH or DTT at pH 6 in PBS at a specific time point and $F_{t,b}$ is the fluorescence of PEGylated 5 nm AuNPs mixed with AF647-labeled antibodies at a specific time point at pH 6; the concentrations of gold nanoparticles and antibodies were matched with their concentrations in 5 nm aEGFR-AuNP conjugates; and $F_{t,0}$ is the fluorescence of 5 nm aEGFR-AuNPs at pH 6 at a specific time point.

https://doi.org/10.1021/acsnano.0c08128
ACS Nano 2021, 15, 9495−9508

Statistical Analysis. ANOVA with Tukey's multiple comparison tests was used to compare the means of more than two groups simultaneously. A p-value of less than 0.05 was considered statistically significant. Pearson's correlation was used to evaluate a linear signal correlation between two variables.

ASSOCIATED CONTENT

Supporting Information

The Supporting Information is available free of charge at https://pubs.acs.org/doi/10.1021/acsnano.0c08128.

TEM of 5 nm AuNP conjugates; cell viability assay; absorbance spectra of isolated and aggregated 5 nm AuNPs in solution; a plot with the ratio of the number of voxels with isolated Ab fluorescence to the voxels with colocalized TPL from AuNP clusters and Abs at different time points; time-correlated single-photon count data analysis; TEM images of cells labeled with 5 nm aEGFR-AuNPs; UV−vis−NIR spectra, DLS and TEM of 5 nm aEGFR-AuNPs following incubation with either GSH or DTT; and *in vivo* two-photon microscopy image of A431 cells labeled with 5 nm aEGFR-AuNPs (PDF)

AUTHOR INFORMATION

Corresponding Authors

Tomasz Zal − *Department of Leukemia, The University of Texas M.D. Anderson Cancer Center, Houston, Texas 77030, United States*; Email: tzal@mdanderson.org

Konstantin V. Sokolov − *Department of Bioengineering, Rice University, Houston, Texas 77005, United States; Department of Imaging Physics, The University of Texas M.D. Anderson Cancer Center, Houston, Texas 77030, United States*; orcid.org/0000-0002-0198-2005; Email: ksokolov@mdanderson.org

Author

Sangheon Han − *Department of Bioengineering, Rice University, Houston, Texas 77005, United States; Department of Imaging Physics, The University of Texas M.D. Anderson Cancer Center, Houston, Texas 77030, United States*; orcid.org/0000-0003-0626-3162

Complete contact information is available at: https://pubs.acs.org/10.1021/acsnano.0c08128

Notes

The authors declare the following competing financial interest(s): K.V. Sokolov has an ownership interest in Nanohybrids, LLC. Other authors have no conflicts of interest related to this article.

ACKNOWLEDGMENTS

The work was supported, in part, by grants from the NIH (R01EB008101) and CPRIT (RP170314). We also acknowledge CCSG grant NIH P30CA016672, the High-Resolution Electron Microscopy Facility for the use of transmission electron microscopy, and Advanced Microscopy Core Facility for lifetime two-photon microscopy and image analysis. We also would like to thank Kelly M. Kage, Medical Illustrator at MD Anderson Cancer Center, for creating graphics for Figure 8.

REFERENCES

(1) Kim, Y.; Tewari, M.; Pajerowski, J. D.; Cai, S.; Sen, S.; Williams, J. H.; Sirsi, S. R.; Lutz, G. J.; Discher, D. E. Polymersome Delivery of siRNA and Antisense Oligonucleotides. *J. Controlled Release* **2009**, *134* (2), 132−40.

(2) Kabanov, A. V.; Vinogradov, S. V. Nanogels as Pharmaceutical Carriers: Finite Networks of Infinite Capabilities. *Angew. Chem., Int. Ed.* **2009**, *48* (30), 5418−29.

(3) Hickey, R. J.; Koski, J.; Meng, X.; Riggleman, R. A.; Zhang, P.; Park, S. J. Size-Controlled Self-Assembly of Superparamagnetic Polymersomes. *ACS Nano* **2014**, *8* (1), 495−502.

(4) Carugo, D.; Bottaro, E.; Owen, J.; Stride, E.; Nastruzzi, C. Liposome Production by Microfluidics: Potential and Limiting Factors. *Sci. Rep.* **2016**, *6*, 25876.

(5) Sun, X.; Yan, X.; Jacobson, O.; Sun, W.; Wang, Z.; Tong, X.; Xia, Y.; Ling, D.; Chen, X. Improved Tumor Uptake by Optimizing Liposome Based RES Blockade Strategy. *Theranostics* **2017**, *7* (2), 319−328.

(6) Lovell, J. F.; Jin, C. S.; Huynh, E.; Jin, H.; Kim, C.; Rubinstein, J. L.; Chan, W. C.; Cao, W.; Wang, L. V.; Zheng, G. Porphysome Nanovesicles Generated by Porphyrin Bilayers for Use as Multimodal Biophotonic Contrast Agents. *Nat. Mater.* **2011**, *10* (4), 324−32.

(7) Carter, K. A.; Shao, S.; Hoopes, M. I.; Luo, D.; Ahsan, B.; Grigoryants, V. M.; Song, W.; Huang, H.; Zhang, G.; Pandey, R. K.; Geng, J.; Pfeifer, B. A.; Scholes, C. P.; Ortega, J.; Karttunen, M.; Lovell, J. F. Porphyrin-Phospholipid Liposomes Permeabilized by Near-Infrared Light. *Nat. Commun.* **2014**, *5*, 3546.

(8) Torchilin, V. P. Recent Advances with Liposomes as Pharmaceutical Carriers. *Nat. Rev. Drug Discovery* **2005**, *4* (2), 145−60.

(9) Tong, S.; Quinto, C. A.; Zhang, L.; Mohindra, P.; Bao, G. Size-Dependent Heating of Magnetic Iron Oxide Nanoparticles. *ACS Nano* **2017**, *11* (7), 6808−6816.

(10) Walkey, C. D.; Olsen, J. B.; Song, F.; Liu, R.; Guo, H.; Olsen, D. W.; Cohen, Y.; Emili, A.; Chan, W. C. Protein Corona Fingerprinting Predicts the Cellular Interaction of Gold and Silver Nanoparticles. *ACS Nano* **2014**, *8* (3), 2439−55.

(11) Sokolov, K.; Follen, M.; Aaron, J.; Pavlova, I.; Malpica, A.; Lotan, R.; Richards-Kortum, R. Real-Time Vital Optical Imaging of Precancer Using Anti-Epidermal Growth Factor Receptor Antibodies Conjugated to Gold Nanoparticles. *Cancer Res.* **2003**, *63* (9), 1999−2004.

(12) Chan, W. C.; Nie, S. Quantum Dot Bioconjugates for Ultrasensitive Nonisotopic Detection. *Science* **1998**, *281* (5385), 2016−8.

(13) Albanese, A.; Tang, P. S.; Chan, W. C. The Effect of Nanoparticle Size, Shape, and Surface Chemistry on Biological Systems. *Annu. Rev. Biomed. Eng.* **2012**, *14*, 1−16.

(14) Nune, S. K.; Chanda, N.; Shukla, R.; Katti, K.; Kulkarni, R. R.; Thilakavathi, S.; Mekapothula, S.; Kannan, R.; Katti, K. V. Green Nanotechnology from Tea: Phytochemicals in Tea as Building Blocks for Production of Biocompatible Gold Nanoparticles. *J. Mater. Chem.* **2009**, *19* (19), 2912−2920.

(15) Cavigli, L.; Centi, S.; Borri, C.; Tortoli, P.; Panettieri, I.; Streit, I.; Ciofini, D.; Magni, G.; Rossi, F.; Siano, S.; Ratto, F.; Pini, R. 1064-Nm-Resonant Gold Nanorods for Photoacoustic Theranostics within Permissible Exposure Limits. *J. Biophotonics* **2019**, *12* (10), No. e201900082.

(16) Zhang, D.; Gokce, B.; Barcikowski, S. Laser Synthesis and Processing of Colloids: Fundamentals and Applications. *Chem. Rev.* **2017**, *117* (5), 3990−4103.

(17) Rabiee, N.; Yaraki, M. T.; Garakani, S. M.; Garakani, S. M.; Ahmadi, S.; Lajevardi, A.; Bagherzadeh, M.; Rabiee, M.; Tayebi, L.; Tahriri, M.; Hamblin, M. R. Recent Advances in Porphyrin-Based Nanocomposites for Effective Targeted Imaging and Therapy. *Biomaterials* **2020**, *232*, 119707.

(18) Dadfar, S. M.; Roemhild, K.; Drude, N. I.; von Stillfried, S.; Knüchel, R.; Kiessling, F.; Lammers, T. Iron Oxide Nanoparticles:

Diagnostic, Therapeutic and Theranostic Applications. *Adv. Drug Delivery Rev.* **2019**, *138*, 302−325.
(19) Cai, X.; Liu, B. Aggregation-Induced Emission: Recent Advances in Materials and Biomedical Applications. *Angew. Chem., Int. Ed.* **2020**, *59* (25), 9868−9886.
(20) Bort, G.; Lux, F.; Dufort, S.; Crémillieux, Y.; Verry, C.; Tillement, O. EPR-Mediated Tumor Targeting Using Ultrasmall-Hybrid Nanoparticles: From Animal to Human with Theranostic AGuIX Nanoparticles. *Theranostics* **2020**, *10* (3), 1319−1331.
(21) Milanesi, A.; Magni, G.; Centi, S.; Schifino, G.; Aluigi, A.; Khlebtsov, B. N.; Cavigli, L.; Barucci, A.; Khlebtsov, N. G.; Ratto, F.; Rossi, F.; Pini, R. Optically Activated and Interrogated Plasmonic Hydrogels for Applications in Wound Healing. *J. Biophotonics* **2020**, *13* (9), No. e202000135.
(22) Cui, S.; Yin, D.; Chen, Y.; Di, Y.; Chen, H.; Ma, Y.; Achilefu, S.; Gu, Y. *In Vivo* Targeted Deep-Tissue Photodynamic Therapy Based on Near-Infrared Light Triggered Upconversion Nanoconstruct. *ACS Nano* **2013**, *7* (1), 676−88.
(23) Spicer, C. D.; Jumeaux, C.; Gupta, B.; Stevens, M. M. Peptide and Protein Nanoparticle Conjugates: Versatile Platforms for Biomedical Applications. *Chem. Soc. Rev.* **2018**, *47* (10), 3574−3620.
(24) Sivaram, A. J.; Wardiana, A.; Howard, C. B.; Mahler, S. M.; Thurecht, K. J. Recent Advances in the Generation of Antibody−Nanomaterial Conjugates. *Adv. Healthcare Mater.* **2018**, *7* (1), 1700607.
(25) Sperling, R. A.; Rivera Gil, P.; Zhang, F.; Zanella, M.; Parak, W. J. Biological Applications of Gold Nanoparticles. *Chem. Soc. Rev.* **2008**, *37* (9), 1896−908.
(26) Kannan, R.; Rahing, V.; Cutler, C.; Pandrapragada, R.; Katti, K. K.; Kattumuri, V.; Robertson, J. D.; Casteel, S. J.; Jurisson, S.; Smith, C.; Boote, E.; Katti, K. V. Nanocompatible Chemistry toward Fabrication of Target-Specific Gold Nanoparticles. *J. Am. Chem. Soc.* **2006**, *128* (35), 11342−3.
(27) Gómez-Vallejo, V.; Puigivila, M.; Plaza-García, S.; Szczupak, B.; Piñol, R.; Murillo, J. L.; Sorribas, V.; Lou, G.; Veintemillas, S.; Ramos-Cabrer, P.; Llop, J.; Millán, A. PEG-Copolymer-Coated Iron Oxide Nanoparticles That Avoid the Reticuloendothelial System and Act as Kidney MRI Contrast Agents. *Nanoscale* **2018**, *10* (29), 14153−14164.
(28) Yu, M.; Zheng, J. Clearance Pathways and Tumor Targeting of Imaging Nanoparticles. *ACS Nano* **2015**, *9* (7), 6655−6674.
(29) Hadipour Moghaddam, S. P.; Mohammadpour, R.; Ghandehari, H. *In Vitro* and *in Vivo* Evaluation of Degradation, Toxicity, Biodistribution, and Clearance of Silica Nanoparticles as a Function of Size, Porosity, Density, and Composition. *J. Controlled Release* **2019**, *311*−*312*, 1−15.
(30) Sancey, L.; Kotb, S.; Truillet, C.; Appaix, F.; Marais, A.; Thomas, E.; van der Sanden, B.; Klein, J. P.; Laurent, B.; Cottier, M.; Antoine, R.; Dugourd, P.; Panczer, G.; Lux, F.; Perriat, P.; Motto-Ros, V.; Tillement, O. Long-Term *in Vivo* Clearance of Gadolinium-Based AGuIX Nanoparticles and Their Biocompatibility after Systemic Injection. *ACS Nano* **2015**, *9* (3), 2477−88.
(31) Jenkins, J. T.; Halaney, D. L.; Sokolov, K. V.; Ma, L. L.; Shipley, H. J.; Mahajan, S.; Louden, C. L.; Asmis, R.; Milner, T. E.; Johnston, K. P.; Feldman, M. D. Excretion and Toxicity of Gold-Iron Nanoparticles. *Nanomedicine* **2013**, *9* (3), 356−65.
(32) Sindhwani, S.; Syed, A. M.; Ngai, J.; Kingston, B. R.; Maiorino, L.; Rothschild, J.; MacMillan, P.; Zhang, Y.; Rajesh, N. U.; Hoang, T.; Wu, J. L. Y.; Wilhelm, S.; Zilman, A.; Gadde, S.; Sulaiman, A.; Ouyang, B.; Lin, Z.; Wang, L.; Egeblad, M.; Chan, W. C. W. The Entry of Nanoparticles into Solid Tumours. *Nat. Mater.* **2020**, *19* (5), 566−575.
(33) Liu, L. Y.; Ma, X.-Z.; Ouyang, B.; Ings, D. P.; Marwah, S.; Liu, J.; Chen, A. Y.; Gupta, R.; Manuel, J.; Chen, X.-C.; Gage, B. K.; Cirlan, I.; Khuu, N.; Chung, S.; Camat, D.; Cheng, M.; Sekhon, M.; Zagorovsky, K.; Abdou Mohamed, M. A.; Thoeni, C.; et al. Nanoparticle Uptake in a Spontaneous and Immunocompetent Woodchuck Liver Cancer Model. *ACS Nano* **2020**, *14* (4), 4698−4715.
(34) Lazarovits, J.; Sindhwani, S.; Tavares, A. J.; Zhang, Y.; Song, F.; Audet, J.; Krieger, J. R.; Syed, A. M.; Stordy, B.; Chan, W. C. W. Supervised Learning and Mass Spectrometry Predicts the *in Vivo* Fate of Nanomaterials. *ACS Nano* **2019**, *13* (7), 8023−8034.
(35) Duncan, R.; Richardson, S. C. Endocytosis and Intracellular Trafficking as Gateways for Nanomedicine Delivery: Opportunities and Challenges. *Mol. Pharmaceutics* **2012**, *9* (9), 2380−402.
(36) Feliu, N.; Docter, D.; Heine, M.; Del Pino, P.; Ashraf, S.; Kolosnjaj-Tabi, J.; Macchiarini, P.; Nielsen, P.; Alloyeau, D.; Gazeau, F.; Stauber, R. H.; Parak, W. J. *In Vivo* Degeneration and the Fate of Inorganic Nanoparticles. *Chem. Soc. Rev.* **2016**, *45* (9), 2440−57.
(37) Nazarenus, M.; Zhang, Q.; Soliman, M. G.; Del Pino, P.; Pelaz, B.; Carregal-Romero, S.; Rejman, J.; Rothen-Rutishauser, B.; Clift, M. J.; Zellner, R.; Nienhaus, G. U.; Delehanty, J. B.; Medintz, I. L.; Parak, W. J. *In Vitro* Interaction of Colloidal Nanoparticles with Mammalian Cells: What Have We Learned Thus Far? *Beilstein J. Nanotechnol.* **2014**, *5*, 1477−90.
(38) Larson, T. A.; Joshi, P. P.; Sokolov, K. Preventing Protein Adsorption and Macrophage Uptake of Gold Nanoparticles *via* a Hydrophobic Shield. *ACS Nano* **2012**, *6* (10), 9182−90.
(39) Kreyling, W. G.; Abdelmonem, A. M.; Ali, Z.; Alves, F.; Geiser, M.; Haberl, N.; Hartmann, R.; Hirn, S.; de Aberasturi, D. J.; Kantner, K.; Khadem-Saba, G.; Montenegro, J. M.; Rejman, J.; Rojo, T.; de Larramendi, I. R.; Ufartes, R.; Wenk, A.; Parak, W. J. *In Vivo* Integrity of Polymer-Coated Gold Nanoparticles. *Nat. Nanotechnol.* **2015**, *10* (7), 619−23.
(40) Carrillo-Carrion, C.; Bocanegra, A. I.; Arnaiz, B.; Feliu, N.; Zhu, D.; Parak, W. J. Triple-Labeling of Polymer-Coated Quantum Dots and Adsorbed Proteins for Tracing Their Fate in Cell Cultures. *ACS Nano* **2019**, *13* (4), 4631−4639.
(41) Han, S.; Bouchard, R.; Sokolov, K. V. Molecular Photoacoustic Imaging with Ultra-Small Gold Nanoparticles. *Biomed. Opt. Express* **2019**, *10* (7), 3472−3483.
(42) Phillips, E.; Penate-Medina, O.; Zanzonico, P. B.; Carvajal, R. D.; Mohan, P.; Ye, Y.; Humm, J.; Gonen, M.; Kalaigian, H.; Schoder, H.; Strauss, H. W.; Larson, S. M.; Wiesner, U.; Bradbury, M. S. Clinical Translation of an Ultrasmall Inorganic Optical-PET Imaging Nanoparticle Probe. *Sci. Transl. Med.* **2014**, *6* (260), 260ra149.
(43) Tang, R.; Xue, J.; Xu, B.; Shen, D.; Sudlow, G. P.; Achilefu, S. Tunable Ultrasmall Visible-To-Extended Near-Infrared Emitting Silver Sulfide Quantum Dots for Integrin-Targeted Cancer Imaging. *ACS Nano* **2015**, *9* (1), 220−30.
(44) Ernsting, M. J.; Murakami, M.; Roy, A.; Li, S. D. Factors Controlling the Pharmacokinetics, Biodistribution and Intratumoral Penetration of Nanoparticles. *J. Controlled Release* **2013**, *172* (3), 782−94.
(45) Semmler-Behnke, M.; Kreyling, W. G.; Lipka, J.; Fertsch, S.; Wenk, A.; Takenaka, S.; Schmid, G.; Brandau, W. Biodistribution of 1.4- and 18-Nm Gold Particles in Rats. *Small* **2008**, *4* (12), 2108−11.
(46) Kumar, S.; Aaron, J.; Sokolov, K. Directional Conjugation of Antibodies to Nanoparticles for Synthesis of Multiplexed Optical Contrast Agents with Both Delivery and Targeting Moieties. *Nat. Protoc.* **2008**, *3* (2), 314−20.
(47) Han, F.; Guan, Z.; Tan, T. S.; Xu, Q.-H. Size-Dependent Two-Photon Excitation Photoluminescence Enhancement in Coupled Noble-Metal Nanoparticles. *ACS Appl. Mater. Interfaces* **2012**, *4* (9), 4746−4751.
(48) Borglin, J.; Guldbrand, S.; Evenbratt, H.; Kirejev, V.; Gronbeck, H.; Ericson, M. B. Insights on Proximity Effect and Multiphoton Induced Luminescence from Gold Nanospheres in Far Field Optical Microscopy. *Appl. Phys. Lett.* **2015**, *107*, 234101.
(49) Olesiak-Banska, J.; Waszkielewicz, M.; Obstarczyk, P.; Samoc, M. Two-Photon Absorption and Photoluminescence of Colloidal Gold Nanoparticles and Nanoclusters. *Chem. Soc. Rev.* **2019**, *48* (15), 4087−4117.
(50) Wang, H.; Huff, T. B.; Zweifel, D. A.; He, W.; Low, P. S.; Wei, A.; Cheng, J. X. *In Vitro* and *In Vivo* Two-Photon Luminescence Imaging of Single Gold Nanorods. *Proc. Natl. Acad. Sci. U. S. A.* **2005**, *102* (44), 15752−6.

https://doi.org/10.1021/acsnano.0c08128
ACS Nano 2021, 15, 9495−9508

(51) Durr, N. J.; Larson, T.; Smith, D. K.; Korgel, B. A.; Sokolov, K.; Ben-Yakar, A. Two-Photon Luminescence Imaging of Cancer Cells Using Molecularly Targeted Gold Nanorods. *Nano Lett.* **2007**, *7* (4), 941−5.
(52) Gao, N.; Chen, Y.; Li, L.; Guan, Z.; Zhao, T.; Zhou, N.; Yuan, P.; Yao, S. Q.; Xu, Q.-H. Shape-Dependent Two-Photon Photoluminescence of Single Gold Nanoparticles. *J. Phys. Chem. C* **2014**, *118* (25), 13904−13911.
(53) Au, L.; Zhang, Q.; Cobley, C. M.; Gidding, M.; Schwartz, A. G.; Chen, J.; Xia, Y. Quantifying the Cellular Uptake of Antibody-Conjugated Au Nanocages by Two-Photon Microscopy and Inductively Coupled Plasma Mass Spectrometry. *ACS Nano* **2010**, *4* (1), 35−42.
(54) Yuan, P.; Ma, R.; Guan, Z.; Gao, N.; Xu, Q.-H. Tuning Two-Photon Photoluminescence of Gold Nanoparticle Aggregates with DNA and Its Application as Turn-On Photoluminescence Probe for DNA Sequence Detection. *ACS Appl. Mater. Interfaces* **2014**, *6* (15), 13149−13156.
(55) Aaron, J.; Travis, K.; Harrison, N.; Sokolov, K. Dynamic Imaging of Molecular Assemblies in Live Cells Based on Nanoparticle Plasmon Resonance Coupling. *Nano Lett.* **2009**, *9* (10), 3612−8.
(56) Guan, Z.; Gao, N.; Jiang, X. F.; Yuan, P.; Han, F.; Xu, Q. H. Huge Enhancement in Two-Photon Photoluminescence of Au Nanoparticle Clusters Revealed by Single-Particle Spectroscopy. *J. Am. Chem. Soc.* **2013**, *135* (19), 7272−7.
(57) Horvath, H. Gustav Mie and the Scattering and Absorption of Light by Particles: Historic Developments and Basics. *J. Quant. Spectrosc. Radiat. Transfer* **2009**, *110* (11), 787−799.
(58) Arbouet, A.; Christofilos, D.; Del Fatti, N.; Vallée, F.; Huntzinger, J. R.; Arnaud, L.; Billaud, P.; Broyer, M. Direct Measurement of the Single-Metal-Cluster Optical Absorption. *Phys. Rev. Lett.* **2004**, *93* (12), 127401.
(59) Tcherniak, A.; Ha, J. W.; Dominguez-Medina, S.; Slaughter, L. S.; Link, S. Probing a Century Old Prediction One Plasmonic Particle at a Time. *Nano Lett.* **2010**, *10* (4), 1398−404.
(60) Zhang, Y.; Yu, J.; Birch, D. J.; Chen, Y. Gold Nanorods for Fluorescence Lifetime Imaging in Biology. *J. Biomed. Opt.* **2010**, *15* (2), 020504.
(61) Suarasan, S.; Licarete, E.; Astilean, S.; Craciun, A. M. Probing Cellular Uptake and Tracking of Differently Shaped Gelatin-Coated Gold Nanoparticles Inside of Ovarian Cancer Cells by Two-Photon Excited Photoluminescence Analyzed by Fluorescence Lifetime Imaging (FLIM). *Colloids Surf., B* **2018**, *166*, 135−143.
(62) Imura, K.; Nagahara, T.; Okamoto, H. Near-Field Two-Photon-Induced Photoluminescence from Single Gold Nanorods and Imaging of Plasmon Modes. *J. Phys. Chem. B* **2005**, *109* (27), 13214−20.
(63) Yokoyama, T.; Tam, J.; Kuroda, S.; Scott, A. W.; Aaron, J.; Larson, T.; Shanker, M.; Correa, A. M.; Kondo, S.; Roth, J. A.; Sokolov, K.; Ramesh, R. EGFR-Targeted Hybrid Plasmonic Magnetic Nanoparticles Synergistically Induce Autophagy and Apoptosis in Non-Small Cell Lung Cancer Cells. *PLoS One* **2011**, *6* (11), No. e25507.
(64) Cupic, K. I.; Rennick, J. J.; Johnston, A. P.; Such, G. K. Controlling Endosomal Escape Using Nanoparticle Composition: Current Progress and Future Perspectives. *Nanomedicine (London, U. K.)* **2019**, *14* (2), 215−223.
(65) Kumar, S.; Harrison, N.; Richards-Kortum, R.; Sokolov, K. Plasmonic Nanosensors for Imaging Intracellular Biomarkers in Live Cells. *Nano Lett.* **2007**, *7* (5), 1338−43.
(66) Behr, J.-P. The Proton Sponge: A Trick to Enter Cells the Viruses Did Not Exploit. *CHIMIA Int. J. Chem.* **1997**, *51*, 34−36.
(67) Yu, G. S.; Bae, Y. M.; Choi, H.; Kong, B.; Choi, I. S.; Choi, J. S. Synthesis of PAMAM Dendrimer Derivatives with Enhanced Buffering Capacity and Remarkable Gene Transfection Efficiency. *Bioconjugate Chem.* **2011**, *22* (6), 1046−55.
(68) Piella, J.; Bastús, N. G.; Puntes, V. Size-Controlled Synthesis of Sub-10-Nanometer Citrate-Stabilized Gold Nanoparticles and Related Optical Properties. *Chem. Mater.* **2016**, *28* (4), 1066−1075.
(69) Reifarth, M.; Hoeppener, S.; Schubert, U. S. Uptake and Intracellular Fate of Engineered Nanoparticles in Mammalian Cells: Capabilities and Limitations of Transmission Electron Microscopy—Polymer-Based Nanoparticles. *Adv. Mater.* **2018**, *30* (9), 1703704.
(70) Reimers, J. R.; Ford, M.; Marcuccio, S. M.; Ulstrup, J.; Hush, N. S. Competition of van der Waals and Chemical Forces on Gold−Sulfur Surfaces and Nanoparticles. *Nat. Rev. Chem.* **2017**, *1*, 0017.
(71) Smith, C. V.; Jones, D. P.; Guenthner, T. M.; Lash, L. H.; Lauterburg, B. H. Compartmentation of Glutathione: Implications for the Study of Toxicity and Disease. *Toxicol. Appl. Pharmacol.* **1996**, *140* (1), 1−12.
(72) Li, N.; Larson, T.; Nguyen, H. H.; Sokolov, K. V.; Ellington, A. D. Directed Evolution of Gold Nanoparticle Delivery to Cells. *Chem. Commun. (Cambridge, U. K.)* **2010**, *46* (3), 392−4.
(73) Sato, K.; Hosokawa, K.; Maeda, M. Non-Cross-Linking Gold Nanoparticle Aggregation as a Detection Method for Single-Base Substitutions. *Nucleic Acids Res.* **2005**, *33* (1), e4−e4.
(74) Moaseri, E.; Stover, R. J.; Changalvaie, B.; Cepeda, A. J.; Truskett, T. M.; Sokolov, K. V.; Johnston, K. P. Control of Primary Particle Spacing in Gold Nanoparticle Clusters for Both High NIR Extinction and Full Reversibility. *Langmuir* **2017**, *33* (14), 3413−3426.
(75) Chanana, M.; Rivera Gil, P.; Correa-Duarte, M. A.; Liz-Marzan, L. M.; Parak, W. J. Physicochemical Properties of Protein-Coated Gold Nanoparticles in Biological Fluids and Cells before and after Proteolytic Digestion. *Angew. Chem., Int. Ed.* **2013**, *52* (15), 4179−83.
(76) Yoon, S. J.; Murthy, A.; Johnston, K. P.; Sokolov, K. V.; Emelianov, S. Y. Thermal Stability of Biodegradable Plasmonic Nanoclusters in Photoacoustic Imaging. *Opt. Express* **2012**, *20* (28), 29479−87.
(77) Kim, T.; Lee, C.-H.; Joo, S.-W.; Lee, K. Kinetics of Gold Nanoparticle Aggregation: Experiments and Modeling. *J. Colloid Interface Sci.* **2008**, *318* (2), 238−243.
(78) Haiss, W.; Thanh, N. T.; Aveyard, J.; Fernig, D. G. Determination of Size and Concentration of Gold Nanoparticles from UV-Vis Spectra. *Anal. Chem.* **2007**, *79* (11), 4215−21.

https://doi.org/10.1021/acsnano.0c08128
ACS Nano 2021, 15, 9495−9508